Ceramics International xxx (xxxx) xxx

Contents lists available at ScienceDirect

Ceramics International

journal homepage: www.elsevier.com/locate/ceramint

Machine learning-driven prediction of optical and physical properties in lanthanum and gold-doped zinc borotellurite glasses for optoelectronic applications

S.N. Nazrin [a,b,*], Camellia Doroody [c,d,e,f], Liyana Adilla Burhanuddin [g], Neesha Jothi [h], N. Ibrahim [i], Halimah Badioze Zaman [b], M.H.M. Tahir [j], Manzoore Elahi M. Soudagar [k,l,m], S. Ramesh [k], Sagar Shelare [n,o], Shubham Sharma [p,q,r,**]

[a] Strategic Research Institute, Asia Pacific University of Technology and Innovation, 57000 Kuala Lumpur, Malaysia
[b] Institute of Informatics and Computing in Energy (IICE), College of Engineering, Universiti Tenaga Nasional, 43000, Kajang, Selangor, Malaysia
[c] Institute of Sustainable Energy (ISE), Universiti Tenaga Nasional (UNITEN @ The Energy University), Putrajaya Campus, Jalan IKRAM-UNITEN, 43000, Kajang, Selangor, Malaysia
[d] Division of Research & Innovation, Uttaranchal University, Dehradun 248007, India
[e] Zhejiang Xingyu Mechanical and Electrical Technology Company Ltd., Tongqin, Wuyi County, Jinhua, Zhejiang, 311400, China
[f] Division of Research and Development, Lovely Professional University, Phagwara, Punjab, 144411, India
[g] Department of Electronic Systems Engineering (ESE), Malaysia–Japan International Institute of Technology (MJIIT), Universiti Teknologi Malaysia, Malaysia
[h] Department of Computing, College of Computing and Informatics, Universiti Tenaga Nasional (UNITEN), Malaysia
[i] Centre for Mathematical Sciences,Universiti Malaysia Pahang Al-Sultan Abdullah, Lebuh Persiaran Tun Khalil Yaakob, 26300 Kuantan, Pahang, Malaysia
[j] Department of English Language and Literature, Faculty of Languages and Communication, Universiti Pendidikan Sultan Idris, Tanjong Malim, 35900, Perak, Malaysia
[k] Center of Advanced Manufacturing and Materials Processing (AMMP), Faculty of Engineering, University of Malaya, Kuala Lumpur, Malaysia
[l] Chitkara Centre for Research and Development, Chitkara University, Himachal Pradesh, 174103, India
[m] Centre for Promotion of Research, Graphic Era (Deemed to be University), Clement town, Dehradun, India
[n] Department of Applied Chemistry, Priyadarshini College of Engineering, Nagpur, Maharashtra, 440019, India
[o] University Centre for Research and Development, Chandigarh University, Mohali, Punjab, 140413, India
[p] Centre for Research Impact and Outcome, Chitkara University Institute of Engineering and Technology, Chitkara University, Rajpura, 140401, Punjab, India
[q] Department of Technical Sciences, Western Caspian University, Baku, Azerbaijan
[r] Jadara University Research Center, Jadara University, Jordan

ARTICLE INFO

Handling Editor: Dr P. Vincenzini

Keywords:
Energy
Gold oxide
Random forest (RF)
Gradient boosting (GB)
XGBoost (XGB)
Artificial neural networks (ANN)

ABSTRACT

Recent advancements in glass science have focused on optimizing optical and structural properties through the incorporation of rare oxide nanoparticles, such as lanthanum and gold oxide, to enhance transparency, refractive index, and band gap energy for photonic applications. Additionally, the integration of machine learning techniques in material design accelerates the prediction and optimisation of these properties, enabling more efficient discovery and development of advanced glass systems for optoelectronic and photonic devices. The melt-quenching technique was employed to fabricate zinc borotellurite glasses doped with lanthanum oxide and gold oxide. The glass's amorphous nature was confirmed through structural analysis, which detected absorption bands corresponding to TeO_3, BO_4, and BO_3 units. A drop in molar volume with an increase in gold oxide quantity prompted a suggestion for structural reorganisation. Optical investigations indicated an increase in the optical band gap energy and a blue shift in the absorption edge. Four machine learning models—Random Forest, Gradient Boosting, XGBoost, and Artificial Neural Networks—were employed to forecast critical optical and physical parameters, such as refractive index, density, molar volume, optical band gap, and Urbach energy, to expedite the discovery process. This data-driven approach illustrates the transformative capabilities of machine learning in materials science, facilitating the swift modification of glass compositions to enhance optical

* Corresponding author. Strategic Research Institute, Asia Pacific University of Technology and Innovation, 57000 Kuala Lumpur, Malaysia.
** Corresponding author. Centre for Research Impact and Outcome, Chitkara University Institute of Engineering and Technology, Chitkara University, Rajpura, 140401, Punjab, India.
E-mail addresses: nazirulnazrin@ymail.com, nazirul.nidzam@apu.edu.my (S.N. Nazrin), camellia@uniten.edu.my (C. Doroody), Liyanaadilla@utm.my (L.A. Burhanuddin), neesha@uniten.edu.my (N. Jothi), norainii@umpsa.edu.my (N. Ibrahim), haniff.tahir@fbk.upsi.edu.my (M.H.M. Tahir), me.soudagar@gmail.com (M.E.M. Soudagar), ramesh79@um.edu.my (S. Ramesh), sagmech24@gmail.com (S. Shelare), shubham543sharma@gmail.com (S. Sharma).

https://doi.org/10.1016/j.ceramint.2025.04.231
Received 2 January 2025; Received in revised form 30 March 2025; Accepted 18 April 2025
Available online 26 April 2025

performance for photonic and optoelectronic applications. The enhanced optical properties of the synthesized glass system make it a promising candidate for photonic and optoelectronic applications, including **optical fibers, solid-state lasers, and planar waveguides**, where its tunable refractive index and improved transparency can optimize signal transmission and device efficiency. Additionally, the presence of gold oxide nanoparticles suggests potential use in **nonlinear optical devices, photodetectors, and solar energy applications**, as the widened optical band gap and band edge shifts contribute to improved light absorption and energy conversion efficiency.

1. Introduction

Glasses exhibit a transparent quality and are prone to fracture. Several scholars, including Doremus (1973), Elliot and Henn (1990), Feltz (1993), Varshneya (1994), and Shelby and Noonan (1997), defined glass as a solid lacking long-range order, often termed non-crystalline solids. Moreover, the glass is generally manufactured by a process known as melt-quenching. Each glass demonstrates an absence of long-range order or periodic structure and exhibits time-dependent activity (glass transformation behaviour). The behaviour occurs within a temperature range known as the glass transition zone. A glass is characterised as a substance, possibly originating from inorganic, organic, or metallic origins, that has glass transition properties, irrespective of its method of formation [1–5] (see Table 8).

The structure of borate glass was previously investigated using X-ray diffraction, revealing that the pure glass comprises a random network in which each boron atom is connected in a triangle configuration to three oxygen atoms. In 1985, Bray asserted that nuclear magnetic resonance (NMR) confirmed the glassy state of B2O3, characterised by several planar BO3 units distributed randomly inside a three-dimensional network, with each oxygen atom shared across neighbouring BO3 units [6]. Tellurite dioxide is the most stable oxide of tellurium, with a melting point of 733 °C. The intermediary position of tellurium between metals and non-metals has made its stability particularly attractive to many researchers [7,8]. The structure of α-TeO2 is defined as a three-dimensional (3D) framework of TeO4 subunits, with each oxygen atom coordinated by two units, linking in the equatorial position to one tellurium atom and in the axial position to another. The elements O, S, Se, and Te are acknowledged for their capacity to produce monoatomic (primary) glasses, which are basic glasses consisting of a single atomic species. These components can create a vitreous network when chemically amalgamated. They synthesise a binary glass, consisting of two distinct atom types, by amalgamating elements from groups III, IV, or V of the periodic table.

In 2019, Nazrin et al. investigated zinc oxide (ZnO). ZnO functions as a glass stabiliser to yield a superior glass specimen. Moreover, ZnO lowers the melting point and enhances the tendency for glass formation. The addition of ZnO to the glass samples may reduce the optical energy band gap and enhance the refractive index [9]. In late 2019, Halimah et al. asserted that ZnO has distinctive features, enabling its use as an additive in diverse materials and products, such as plastics, ceramics, glass, cement, lubricants, and rubber. This white zinc oxide powder has numerous beneficial applications, especially in the semiconductor industry. Zinc oxide possesses beneficial properties such as high electron mobility, a wide band gap, strong room temperature luminescence, and superior transparency, making it a dependable material [10]. In contrast, lanthanum oxide has a band gap of 4.3 eV and a hexagonal crystal structure, rendering it suitable for several applications, including optoelectronic devices and as a dopant in camera lens glass to enhance sharpness and improve image resolution. Moreover, lanthanum oxide is significant in the fabrication of ceramic superconductors, as the magnetic characteristics of lanthanum can be altered by allowing light to pass through it [11]. A further advantage that may distinguish this element is its categorisation within the intra-4f shell optical transition, which augments its properties relative to other elements in the periodic table [12]. The optical properties of the glass system will fluctuate due to the interaction between the embedded lanthanide nanocrystals and the glass constituents. The aim of integrating rare earth ions and nanoscale materials into the glass samples is to identify and evaluate the changes in the local structure induced by the presence of the dopants.

Heavy-metal oxide glasses are appropriate for photonic devices; hence, glass samples with rare earth nanoparticles are suggested to be doped with the heavy metal element, specifically gold oxide (Au). Heavy metal elements are beneficial because to their high refractive index and broad transparency range, spanning from the visible spectrum to the mid-infrared. The doping of the glass sample with rare earth and heavy metal elements improves its luminescent properties due to the low cutoff phonon energy of the host matrix, which subsequently reduces the non-radiative transitions of the electronic levels of rare earth elements relative to other glasses [13–18]. Alongside the hyperpolarizability of the glass constituents, the integration of metallic oxides is expected to improve both linear and nonlinear optical characteristics. Gold (Au) is incorporated into specific materials to improve the performance of both linear and nonlinear optical properties [19–21]. While lanthanum and gold oxide-doped zinc borotellurite glasses have favourable properties, controlling their composition and comprehending the essential structural and optical changes are complex endeavours. Traditional experimental methods, while essential for characterising glass properties, are arduous and require significant material synthesis [22–25]. To alleviate these limitations, machine learning (ML) techniques have increasingly been employed in materials research for property prediction and optimisation.

In recent years, deep learning (DL) and convolutional neural networks (CNNs) have demonstrated significant potential in predicting material properties, accelerating the discovery and optimisation of advanced functional materials [55–59]. For instance, [55] developed a CNN-autoencoder and random forest model to predict pair correlation functions in borosilicate glasses, demonstrating ML's capability in material property prediction [55]. Similarly, authors in [56] explored DL in material selection and optimisation, while [57] demonstrated physical encoding enhances DL model generalization for refractive indices and elastic properties. Furthermore, [58] introduced an CNN model improving structure-agnostic property predictions. Additionally, [59] demonstrated that ensemble deep graph neural networks enhance material property prediction accuracy. Despite these advancements, ML applications in rare-earth and heavy metal-doped borotellurite glasses remain unexplored. This study represents the first application of ML to predict the optical and physical properties of Lanthanum and Gold-Doped Zinc Borotellurite Glass, providing a data-driven framework for material discovery and optimisation in optoelectronics and photonics.

This study assesses the effectiveness of four machine learning models: Random Forest (RF), Gradient Boosting (GB), XGBoost (XGB), and Artificial Neural Networks (ANN), comparing their predictive accuracy and elucidating their strengths and weaknesses in forecasting essential physical and optical attributes. Incorporating machine learning into the experimental workflow can accelerate the optimisation process, enabling the swift identification of high-performance glasses for advanced optical applications. This demonstrates the revolutionary capacity of machine learning in materials research, offering innovative pathways for future advancements in glass formulation and property development. The study begins by clarifying the experimental methodology and characterisation methodologies. A study of machine learning

models for anticipating and optimizing critical ingredients is presented, highlighting their distinct advantages and limits while demonstrating how ML can accelerate the development of new glass compositions with improved optical properties. The report finally explores the wider ramifications of incorporating machine learning into materials science and proposes directions for additional research. This presents an innovative approach to glass optimisation and a framework that has the potential to revolutionise material design across various scientific disciplines.

2. Experimental procedure

A series of pentanary borotellurite glasses were successfully synthesized having the following chemical composition: (TeO2)0.7 (B2O3) 0.30.7 (ZnO)0.3}0.96 (La NPs)0.04]1-y (Au2O3)y, with y values of 0.0010, 0.0015, 0.0020, 0.0025, and 0.0030 M fractions. Boron oxide (B2O3, 97.5 %, Alfa Aesar), tellurium dioxide (TeO2, 99.99 %, Alfa Aesar), zinc oxide (ZnO, 99.99 %, Alfa Aesar), lanthanum oxide nanoparticles (La2O3, 99.99 %, Nanostructured & Amorphous Materials, Inc.), and gold oxide (Au2O3, 99.99 %, Alfa Aesar) were employed in powdered form for the production of glass samples. Accurate amounts of powdered ingredients were measured with an electronic digital balance, exhibiting an accuracy of ±0.0001 g, and thereafter transferred into a crucible. The crucible was subsequently positioned within the electrical furnace. Two furnaces were employed for the production of glass samples. The furnace temperature was set at 400 °C. The major objective of the original boiler was to remove the water content from the chemicals, so enabling their degradation and interaction. After a 60-min period in the first furnace, the crucible was transferred to the second furnace, which functioned at a temperature of 900 °C. The second furnace aimed to expedite the melting and reaction of the chemicals, thus reducing their loss via evaporation. The crucible was situated in the second furnace for 120 min. Concurrently, the mould was preheated to 400 °C in the first furnace to alleviate thermal shock to the samples throughout the ensuing casting process. A considerable temperature difference between the molten glass and the moulds will generate thermal stress in the glass samples. Glasses exposed to substantial thermal stress are unstable and may shatter into shards [5]. After the execution of these two procedures over 120 min, the melt in the crucible was considered a homogeneous molten liquid and was immediately cast into the prepared stainless-steel cylinder moulds. This approach was implemented to prevent solidification during the quenching process.

The glass specimen with the mould was reinserted into the original furnace and underwent an annealing procedure for around 60 min at 400 °C. Subsequently, the primary furnace was deactivated, and the glass specimen was allowed to cool at room temperature overnight. The glass specimen was then extracted from the mould, labelled, and positioned within the desiccator to safeguard it against humidity. This was executed to eradicate residual stress before initiating the polishing process. The glass samples were polished with sandpaper of increasing grits until both surfaces were flat, smooth, and parallel. The average thickness was determined using a micrometre screw gauge. All samples are clear, transparent, and free of bubbles.

Possible sources of error in the fabrication process include variations in material composition, temperature fluctuations, and handling inconsistencies. To minimize these, a high-precision digital balance (±0.0001 g) ensured accurate weighing of raw materials, while controlled furnace temperatures prevented uneven melting and phase separation. The risk of material loss due to evaporation was reduced by maintaining an optimized melting temperature (900 °C for 120 min). Thermal stress, which can cause cracks, was minimized by preheating the moulds to 400 °C and using a controlled annealing process at the same temperature for 60 min, followed by gradual cooling. Lastly, surface defects from polishing were reduced by using progressively finer sandpaper grits to achieve uniform thickness and smoothness. These steps ensured the glass samples were consistent, stable, and defect-free.

3. Machine learning for the prediction and optimisation of optical and physical properties

Applications of machine learning (ML) in materials science has the capacity to revolutionise the discovery and development of materials with tailored optical and physical properties [22]. This research employed a machine learning algorithm to forecast critical attributes, such as Urbach energy, band gap, and refractive index in glass compositions. The model effectively identified the optimal material composition by analysing a comprehensive data set, focussing on the molar fraction of gold oxide (Au_2O_3) and lanthanum nanoparticles [26].

3.1. Random forest

The Random Forest (RF) model has been utilised to investigate the relationship between synthesis factors and the characterisation of nanoparticles [22]. The results demonstrate that the RF model can accurately forecast synthesis outcomes relative to the other three machine learning models: Linear Regression, Adaboost, and XGBoost. SHAP analysis has been utilised to assess the impact of synthesis parameters on gold nanoparticles, determining the importance of each parameter in the synthesis outcomes. The effectiveness of the RF model mostly arises from an algorithm that is less complex than AdaBoost or XGBoost, yet operating at a higher speed. Moreover, it is less computationally demanding because to its simplicity and lack of boosting. Despite its usefulness, RF presents certain drawbacks, such as the potential for overfitting and selection bias due to insufficient validation data. Random Forest (RF) consists of a collection of independent decision trees, each created from a randomly sampled dataset selected with replacement. Each decision tree randomly selects factors to evaluate at each split and generate a prediction. The mean score of the trees is employed for prediction.

3.2. Artificial neural networks (ANNs)

A feedforward artificial neural network is utilised to address potential non-linear interactions between compositional attributes and optical properties. Some predictive features may exhibit linear correlations, while others may be more complex and require the flexibility of artificial neural networks (ANNs). Artificial Neural Networks (ANNs) are a class of machine learning algorithms designed to emulate the structure and functions of the human brain. Unlike linear regression, artificial neural networks can model complex, non-linear relationships [27].

Fig. 1 demonstrates that our ANN model consists of interconnected layers of artificial neurones. The design consisted of an input layer, two hidden layers utilising ReLU activation functions, and an output layer employing a linear activation function. A dropout layer was implemented between the hidden layers to reduce overfitting. Each neurone receives inputs from preceding neurones, applies a mathematical change (activation function), and transmits a signal to the subsequent layer.

The ANN model was then developed utilising the Adam optimiser and the mean squared error loss function. The training was conducted for 100 epochs with a batch size of 10. Call-backs for early stopping and learning rate reduction were utilised to optimize the training process. Early stopping observed the validation loss and ceased training if no improvement was seen for ten consecutive epochs, reverting to the optimal model weights. The learning rate was reduced by a factor of 0.2 if the validation loss did not improve across five consecutive epochs. The Adam optimiser, which combines the advantages of two established stochastic gradient descent extensions, adjusts the weights at each iteration t based on the following principle:

$$\mathbf{m_t} = \boldsymbol{\beta_1}\mathbf{m_{t-1}} + (\mathbf{1} - \boldsymbol{\beta_1})\mathbf{g_t} \tag{3.1}$$

$$\mathbf{v_t} = \boldsymbol{\beta_2}\mathbf{v_{t-1}} + (\mathbf{1} - \boldsymbol{\beta_2})\mathbf{g_t^2} \tag{3.2}$$

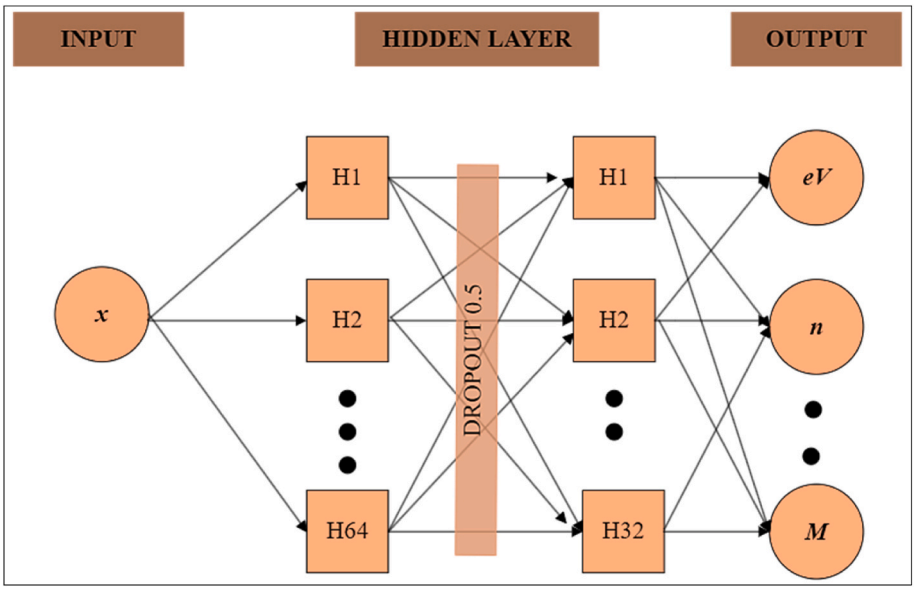

Fig. 1. Relationship between the input, hidden, and output layer in artificial neural networks.

$$\widehat{\mathbf{m}}_t = \frac{\mathbf{m}_t}{\mathbf{1} - \boldsymbol{\beta}_1^t} \tag{3.3}$$

$$\widehat{\mathbf{v}}_t = \frac{\mathbf{v}_t}{\mathbf{1} - \boldsymbol{\beta}_2^t} \tag{3.4}$$

$$\mathbf{w}_{t+1} = \mathbf{w}_t - \frac{\boldsymbol{\eta}}{\sqrt{\widehat{\mathbf{v}}_t} + \boldsymbol{\epsilon}} \widehat{\mathbf{m}}_t \tag{3.5}$$

In this context, η denotes the learning rate, $\beta 1$ and $\beta 2$ represent the decay rates for moment estimations, g_t indicates the gradient of the loss with respect to w at time step t, and ϵ is a minimal constant to prevent division by zero. The training procedure involved adjusting the weights and biases of these connections to minimize the discrepancy between the predicted and actual property values derived from the experimental data. Artificial Neural Networks (ANNs) are advantageous for modelling various functional relationships, particularly in handling non-linear data and achieving high accuracy when effectively trained, especially for complex relationships.

3.3. Gradient Boosting

Gradient Boosting (GB) models have shown superior effectiveness compared to Artificial Neural Networks (ANN) in several applications [25]. Gradient Boosting (GB) demonstrates its effectiveness and potential across several predictive challenges, particularly excelling in regression and classification tasks. This procedure is governed by gradient descent, with each iteration advancing towards the minimisation of the error of a differentiable loss function, such as mean squared error or log loss. Gradient Boosting improves predictions by methodically refining inadequate models using a mathematically precise methodology. Regularisation techniques, including learning rate adjustment, tree depth limitation, and subsampling, enhance the model's generalisation and reduce overfitting. This makes GB particularly suitable for structured data in fields like physics, where complex, non-linear interactions often occur.

3.4. XGBoost

Gradient Boosting, however, has notable downsides, such as a propensity for overfitting, high computing costs, and difficulties with parallelisation. XGBoost (Extreme Gradient Boosting) addresses this issue by incorporating several enhancements that increase speed, including regularisation to mitigate overfitting, an innovative tree pruning algorithm to control tree depth, and a second-order optimisation that employs both gradient and Hessian loss functions to enhance accuracy, as illustrated in Algorithm 1. XGBoost shown enhanced precision in predicting the glass-forming ability of amorphous alloys. A significant breakthrough in XGBoost is its ability to handle sparse data and its inherent management of missing values, making it suitable for real-world scenarios where data incompleteness often presents a challenge [28].

Algorithm 1. XGBoost

1. Initialize the model $F_0(x) = 0$ for all x in the training data
2. for t = 1 to T do:
3. Compute the gradients $g_i(t)$ and Hessians $h_i(t)$ for each instance i:
   $g_i(t) = \partial L(y_i, F_{t-1}(x_i))/\partial F_{t-1}(x_i)$
   $h_i(t) = \partial^2 L(y_i, F_{t-1}(x_i))/\partial F_{t-1}(x_i)^2$
4. Apply regularisation (L1 and L2):
   Adjusted $g_i(t) = g_i(t) + \lambda * F_{t-1}(x_i)$
   Adjusted $h_i(t) = h_i(t) + \alpha$
5. Fit a new decision tree $h_t(x)$ using the gradients and Hessians, limit tree depth to \(\tilde{d}\)
   Prune nodes with gain $< \gamma$ (min loss reduction)
6. Compute the optimal leaf weights $w_j(t)$ for each leaf j in tree h_t:
   $w_j(t) = \arg\min_w \Sigma \{x_i \in R_j\} L(y_i, F_{t-1}(x_i) + w)$
7. Update the model:
   $F_t(x) = F_{t-1}(x) + \eta * h_t(x) * w_j(t)$
8. end for
9. Output the final model $F_t(x)$

We want to identify the optimal solution for each trait prediction challenge by assessing the predictive efficacy of machine learning algorithms. Moreover, the interpretability provides substantial insight into the fundamental link between nanoparticles and the physical and optical properties of glasses.

4. Results and discussions

4.1. Studies related to X-ray diffraction (XRD) and high-resolution transmission electron microscopy (HR-TEM)

Fig. 2 demonstrates that X-ray diffraction (XRD) functions as a non-destructive technique, and the absence of distinct peaks in the XRD patterns of the synthesized glasses signifies a short-range periodic lattice

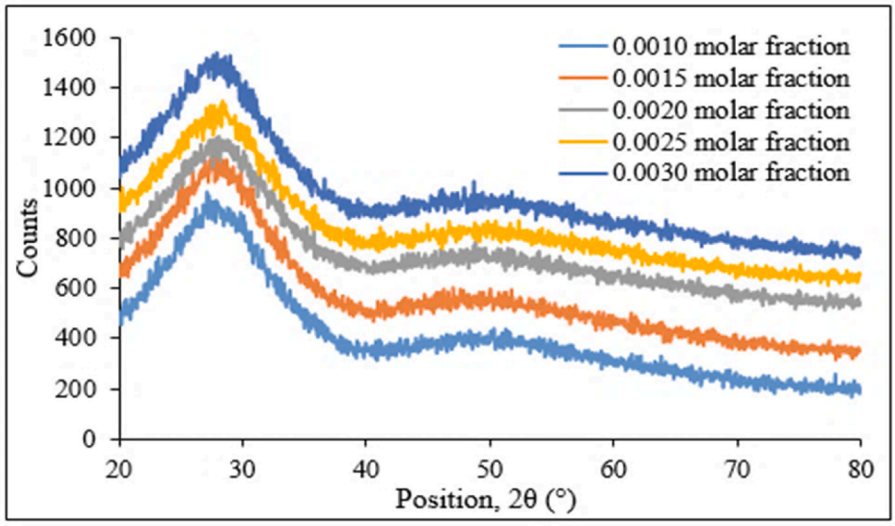

Fig. 2. XRD patterns of $[\{[(TeO_2)_{0.7}\ (B_2O_3)_{0.3}]_{0.7}\ (ZnO)_{0.3}\}_{0.96}\ (La\ NPs)_{0.04}]_{1\text{-}y}\ (Au_2O_3)_y$ glasses.

structure typical of a crystal. The XRD spectra display a prominent hump, indicating that the material is non-crystalline and amorphous in nature [29]. This broad hump arises from the absence of long-range atomic periodicity, which prevents constructive interference and sharp Bragg reflections characteristic of crystalline materials. Instead, the disordered atomic structure results in diffuse scattering, forming a broad peak between 20° and 40° 2θ. The variation in molar fractions (0.0010–0.0030) does not introduce crystallinity, as all spectra retain the amorphous signature, suggesting that the dopant is homogeneously integrated without disrupting the glassy matrix. This confirms that the synthesized material maintains its non-crystalline structure, ensuring its suitability for applications requiring optically transparent and structurally stable glass.

Concurrent HR-TEM investigations were performed to verify the presence of lanthanum nanoparticles within the glass matrix. Fig. 3 depicts the HR-TEM images of zinc borotellurite glass incorporated with lanthanum nanoparticles and gold oxide. The small black spot observed in the HR-TEM image indicates the presence of lanthanum nanoparticles within the glass matrix. Pure lanthanum nanoparticle powder has an average size between 15 and 30 nm [28]. The dimensions of lanthanum nanoparticles, after the incorporation of a gold oxide-doped zinc borotellurite glass system, are quantified at 15.14 nm. This reduction in nanoparticle size can be attributed to the interaction between lanthanum and the surrounding glass matrix, where gold oxide doping influences the nucleation and growth process of lanthanum nanoparticles. The high-resolution imaging further reveals that the nanoparticles are well-dispersed within the amorphous structure, preventing significant agglomeration. This uniform distribution enhances the optical and structural properties of the glass, indicating effective incorporation of lanthanum within the modified zinc borotellurite system.

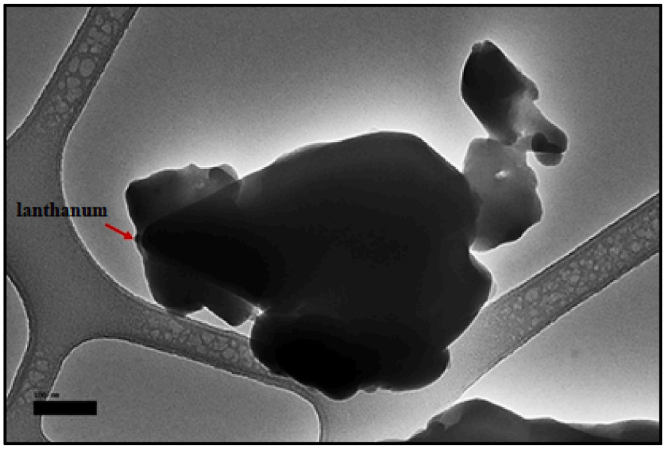

Fig. 3. HR-TEM image of $[\{[(TeO_2)_{0.7}\ (B_2O_3)_{0.3}]_{0.7}\ (ZnO)_{0.3}\}_{0.96}\ (La\ NPs)_{0.04}]_{1\text{-}y}\ (Au_2O_3)_y$ for y = 0.0020 M fraction.

4.2. Fourier transform infrared (FTIR) spectra

FTIR spectroscopy was employed to analyse the functional groups and structural bonding in both amorphous and crystalline materials [27]. FTIR provides insights into the properties of functional groups linked to certain infrared spectra within the glass system. Every material has a unique atomic composition; hence, it is impossible for two compounds to have the same vibrational frequencies [30]. The FTIR spectra of the synthesized glass samples with differing amounts of gold oxide are presented in Fig. 4, and the band assignments are listed in Table 1. Fig. 4 displays a wide band within the wavenumber ranges of 663–669, 1234–1244, and 1338-1352 cm^{-1}. A small absorption band is detected around 1056-1078 cm^{-1}. The structural components of the tellurite

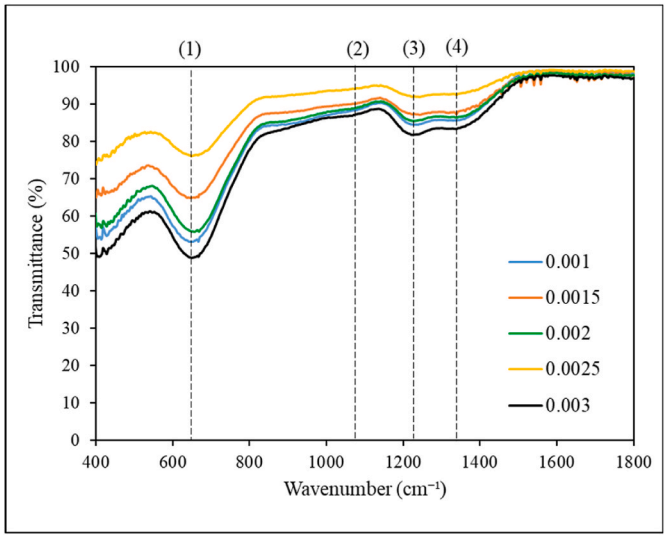

Fig. 4. FTIR spectra of [{[(TeO2)0.7 (B2O3)0.3]0.7 (ZnO)0.3}0.96 (La NPs) 0.04]1-y (Au2O3)y glasses.

Table 1
Functional vibration groups (in cm-1) for [{[(TeO2)0.7 (B2O3)0.3]0.7 (ZnO)0.3}0.96 (La NPs)0.04]1-y (Au2O3)y glasses.

Sample	0.0010	0.0015	0.0020	0.0025	0.0030	Assignments
1	667.37	663.51	669.30	667.37	667.37	Te–O vibration in trigonal pyramid (TeO3) groups [33]
2	1078.21	1076.28	1072.42	1056.99	1066.64	B–O stretching vibration of BO4 units in tri-, tetra-, and penta- borate groups [34]
3	1240.23	1244.09	1234.44	1244.09	1240.23	Trigonal B-O bond stretching vibrations of BO3 units from boroxyl groups [35]
4	1348.24	1338.60	1352.10	1338.60	1338.60	Asymmetric stretching vibrations of the BO3 triangles in metaborate, pyroborate, and ortho-borate units [36]

Structural Unit	Wavenumber Range (cm-1)	Bonding Type	Role in Glass Network	Effect of increasing Au2O3
TeO4 (N4) - Trigonal Bipyramidal	600–650	Bridging Oxygen (BOs)	Forms a strong, interconnected network	Decreases as Au2O3 content increases, leading to depolymerization
TeO3 (N3) - Trigonal Pyramidal	650–700	Non-Bridging Oxygen (NBOs)	Creates structural disorder and modifies network	Increases with Au2O3, reducing rigidity and increasing optical basicity
BO4 - Tetrahedral Boron	1056–1078	Bridging Oxygen (BOs)	Strengthens glass matrix and improves stability	Slight decrease with Au2O3 due to network modification
BO3 - Trigonal Boron	1234–1352	Non-Bridging Oxygen (NBOs)	Reduces connectivity, enhances optical tunability	Increases with Au2O3, promoting structural flexibility and altering optical properties

network consist of trigonal bipyramids, TeO_4, and trigonal pyramids, TeO_3, situated within the absorption band of 600–700 cm^{-1}. The stretching vibration of the TeO_4 group is recognised between 600 and 650 cm^{-1}, while the stretching vibration of the TeO_3 group is detected between 650 and 700 cm^{-1} [31]. The vibrational mode of boron oxide consists of the stretching vibrations of BO_3 and BO_4 units. The active region for B-O bond stretching in tetrahedral BO_4 units is between 800 and 1200 cm^{-1}, while the asymmetric stretching vibration of B-O bonds in BO_3 units is detected in the range of 1200–1600 cm^{-1} [32].

The FTIR spectra in Fig. 4 exhibit a prominent peak at 663-669 cm^{-1}, indicating the presence of the TeO_3 group in the glass system. The breadth of the TeO_3 absorption band signifies an increasing amount of non-bridging oxygen in the glass samples with the augmentation of gold oxide concentration. A small absorption peak at 1056-1078 cm^{-1} is ascribed to the BO_4 units with bridging oxygen. The peaks seen at 1234–1244 and 1338-1352 cm^{-1} in the prepared samples correspond to the stretching vibrations of BO3 units. The FTIR spectra failed to exhibit the absorption band for ZnO, La_2O_3 nanoparticles, and Au_2O_3, due to the complete disintegration of the lattice structures of the zinc, lanthanum nanoparticles, and gold oxide.

This absence suggests that the metal oxides are effectively incorporated into the glass matrix through strong interactions with the borotellurite network, leading to a homogeneous glassy phase. The increase in non-bridging oxygen with rising gold oxide content indicates structural modifications within the tellurite and borate units, which could enhance optical.

The expansion of the FTIR spectra discussion to provide a more detailed explanation of the bonding changes in the presence of gold oxide, supported by earlier studies. The broad band at 663-669 cm-1 corresponds to the presence of TeO3 units, with an increasing intensity as the gold oxide content rises, indicating a structural shift towards more non-bridging oxygen (NBOs). This transition suggests that the incorporation of Au2O3 modifies the tellurite glass network by converting some TeO4 (N4) structural units into TeO3 (N3) pyramidal units, disrupting the connectivity and influencing the optical properties.

Additionally, the absorption band at 1056-1078 cm-1 is associated with BO4 bridging oxygen (BOs), while the peaks at 1234-1244 cm-1 and 1338-1352 cm-1 correspond to BO3 asymmetric stretching vibrations. The observed changes in these peaks suggest that gold oxide influences the borate network by increasing the presence of NBOs, reducing structural rigidity, and enhancing optical basicity. These findings align with previous research indicating that gold oxide acts as a network modifier, promoting depolymerization of the glass structure.

To further strengthen our explanation, we have included a comparison table of N3 and N4 bonding configurations, demonstrating the transformation between bridging and non-bridging oxygen sites as the molar fraction of Au2O3 increases. These structural modifications play a crucial role in determining the optical characteristics of the synthesized glasses, including their refractive index, band gap energy, and polarizability, which are essential for their application in photonics and optoelectronics.

This table highlights how gold oxide (Au2O3) serves as a network modifier, increasing non-bridging oxygen (NBOs) at the expense of bridging oxygen (BOs), leading to a more disordered and optically tunable glass structure. These structural transformations directly impact the refractive index, molar volume, and optical band gap, making the glass suitable for photonics and optoelectronic applications.

4.3. Density and molar volume analysis

The density of glass is a crucial quantity that facilitates the computation of compactness inside the glass system's structure [37]. The density of the synthesized glass samples is analysed using Archimedes' principle at room temperature, as described by Equation (3.6). Simultaneously, the molar volume is calculated by substituting the determined density into Equation (3.7):

$$\rho_{glass} = \frac{W_{air}}{W_{air} - W_{water}} (\rho_{water}) \quad (3.6)$$

$$V_{m=\frac{M_w}{\rho_{glass}}} \quad (3.7)$$

W_air represents the weight of the glass sample in air, W_(water) indicates the weight of the glass sample in water, ρ_(water) is equal to 1 g/cm3, and M_w defines the molecular weight of the glass sample.

The addition of gold oxide to the glass sample caused a structural reconfiguration of the atoms. The alteration of the geometric configuration arises from the incorporation of gold oxide inside the glassy matrix [38]. The evaluated density and molar volume values are displayed in Table 2 and depicted in Fig. 4. The heightened density can be attributed to the superior atomic mass of lanthanum oxide nanoparticles and gold oxide in comparison to the zinc borotellurite-based glasses. The decrease in molar volume is due to the inverse correlation between density and molar volume, as well as the existence of non-bridging oxygen in the glass system [26,37]. Furthermore, the decrease in molar volume may be associated with the reduction in interatomic spacing,

Table 2
Density and molar volume of $[\{[(TeO_2)_{0.7}\ (B_2O_3)_{0.3}]_{0.7}\ (ZnO)_{0.3}\}_{0.96}\ (La\ NPs)_{0.04}]_{1-y}\ (Au_2O_3)_y$ glasses.

Molar fraction, x	Density (g/cm^3)	Molar volume (cm^3/mol)
0.0010	4.3093	29.2082
0.0015	4.3484	28.9488
0.0020	4.3756	28.7917
0.0025	4.4119	28.5775
0.0030	4.4548	28.3248

thus enhancing the stretching force constant of the bonds within the glass network, so facilitating increased compactness and densification of the glasses [38]. Essentially, heightened density enhances the compactness of the glass structure.

The trend observed in Fig. 4 confirms that as the molar fraction of gold oxide increases, the overall compactness of the glass matrix is enhanced due to the introduction of heavier atomic species and stronger interatomic interactions. The densification process reduces free volume within the structure, thereby reinforcing the rigidity of the glass network. This enhanced compactness is a result of reduced bond length and increased bond strength between the constituent elements, leading to a more tightly packed and mechanically robust glass system.

4.4. UV–Vis. Absorption spectroscopy

The optical absorption and the basic absorption edge are critical metrics for assessing the optical properties of materials. These values provide information regarding the band structure and energy gap of amorphous materials [39]. Fig. 5 depicts the optical absorption spectra of glasses infused with different amounts of gold oxide. The absorption spectra display no discernible peak, indicating the glassy state of the glass samples. The characteristics of the fundamental absorption edge are affected by variations in oxygen bonding within the glass matrix [40]. The fundamental absorption edge moves to shorter wavelengths as the concentration of gold oxide in the glass system increases. This may be linked to the heightened rigidity of the resultant glass samples attributable to the inclusion of gold oxide [41].

This shift in the absorption edge can be correlated with variations in the optical band gap energy, which can be evaluated using both direct and indirect transitions. The increase in gold oxide concentration leads to a widening of the optical band gap due to a decrease in non-bridging oxygen atoms, which strengthens the glass network and reduces localized states in the band structure. Urbach energy, which describes the width of the localized states in the band tail, is also affected by this structural modification. A decrease in Urbach energy with increasing gold oxide content suggests a reduction in structural disorder and defect states, contributing to an overall enhancement of the optical stability of the glass.

Furthermore, the refractive index of the glass system is influenced by these structural changes, as higher density and compactness contribute to increased polarizability. The molar refraction (RmR_mRm), which depends on both the refractive index and molar volume, reflects the degree of light interaction with the material. As the gold oxide content increases, a reduction in molar volume enhances the molar refraction and electronic polarizability (αm\alpha_mαm), reinforcing the optical response of the glass. Optical basicity (Λ\LambdaΛ), which measures the ability of the glass network to donate electrons, is also affected by

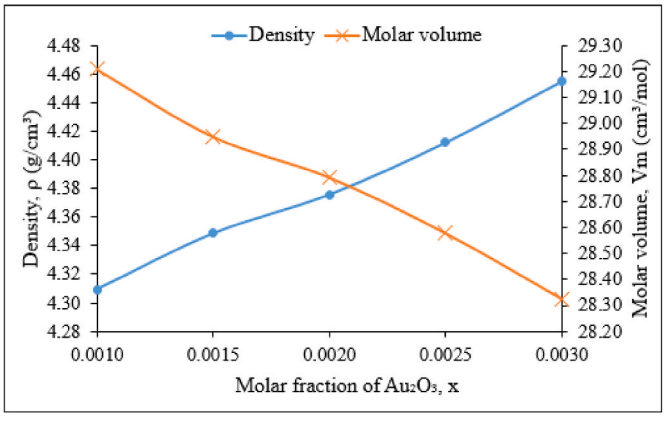

Fig. 5. Density and molar volume of $[\{[(TeO_2)_{0.7}\ (B_2O_3)_{0.3}]_{0.7}\ (ZnO)_{0.3}\}_{0.96}$ (La NPs)$_{0.04}]_{1\text{-}y}$ $(Au_2O_3)_y$ glasses.

gold oxide incorporation. A higher optical basicity value indicates stronger covalent bonding interactions within the glass network, improving its structural integrity.

The metallisation criterion (MMM), which evaluates the transition between insulating and metallic behavior, is another crucial parameter. A decrease in MMM with increasing gold oxide concentration suggests a more insulating nature, further confirming the optical transparency and stability of the material. These optical parameters collectively demonstrate that the incorporation of gold oxide leads to enhanced optical performance by modifying the glass structure, reducing disorder, and increasing overall material stability, making it a potential candidate for optoelectronic applications.

The optical band gap of the glass samples was obtained using the optical absorption spectra. Direct (n = 1/2) and indirect (n = 2) transitions within the band gaps are ascertained according to the theory proposed by Mott and Davis, as seen in Equation (3.8). The absorption coefficient is graphed against photon energy at elevated absorption levels in the ultraviolet band [42,43]:

$$\alpha(\omega) = \frac{B(\hbar\omega - Eopt)^n}{\hbar\omega} \tag{3.8}$$

The optical band gap values for direct and indirect transitions of this glass series are presented in Table 3. Figs. 6 and 7 illustrate the optical band gap of each glass sample by drawing a straight line from the linear portion of the Tauc plot until it intersects with the photon energy axis [44].

Fig. 8 depicts the graph of direct and indirect band gaps. The graphic illustrates two trends: both band gaps rise from a molar fraction of 0.001–0.002 and then decline from 0.002 to 0.003. The augmentation of optical band gaps is associated with the structural reconfiguration of the glass matrix. The augmentation of these parameters may be associated with the elevation of covalency of oxygen ions and the modification of oxygen bond strength inside the glass sample following the integration of gold oxide into the glass matrix. The energised electrons exhibit a stronger coupling to bridging oxygen than to non-bridging oxygen [39]. The diminution of the band gaps can be attributed to the energy transferred from gold oxide to NBO during the electron transition from the ground state to the excited state. The free electron at NBO has surplus energy, allowing it to shift from the valence state to the conduction state, thus reducing the optical energy band gap. The decrease in optical band gaps is attributed to the conversion of TeO4 to TeO3 units and the reduced bonding energies of non-bridging oxygens (NBO) [44].

The Urbach energy values can signify the degree of disorder in amorphous materials. The relationship between the optical absorption coefficient and photon energy near the optical band edge can be employed to ascertain the values of Urbach energy. The Urbach energy values were determined by calculating the reciprocal of the gradient of the ln α against ħω graph using the following relation [45]:

$$\alpha(\omega) = \beta \exp\left(\frac{\hbar\omega}{\Delta E}\right) \tag{3.9}$$

In this context, α(ω) denotes the absorption coefficient, β signifies the constant, ħω indicates the photon energy, and ΔE refers to the Urbach energy.

Table 3
The values of indirect band gap, direct band gap, and Urbach energy for $[\{[(TeO_2)_{0.7}\ (B_2O_3)_{0.3}]_{0.7}\ (ZnO)_{0.3}\}_{0.96}$ (La NPs)$_{0.04}]_{1\text{-}y}$ $(Au_2O_3)_y$ glasses.

Molar fraction, y	Indirect band gap (eV)	Direct band gap (eV)	Urbach energy, ΔE (eV)
0.0010	3.2911	3.4693	0.3458
0.0015	3.3753	3.5372	0.3098
0.0020	3.4480	3.5850	0.3083
0.0025	3.4133	3.5279	0.3111
0.0030	3.2803	3.4759	0.3579

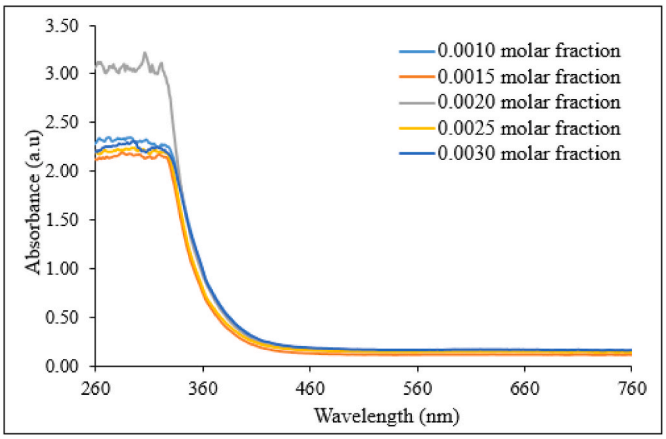

Fig. 6. The optical absorption spectra of $[\{[(TeO_2)_{0.7}\ (B_2O_3)_{0.3}]_{0.7}\ (ZnO)_{0.3}\}_{0.96}\ (La\ NPs)_{0.04}]_{1\text{-}y}\ (Au_2O_3)_y$ glasses.

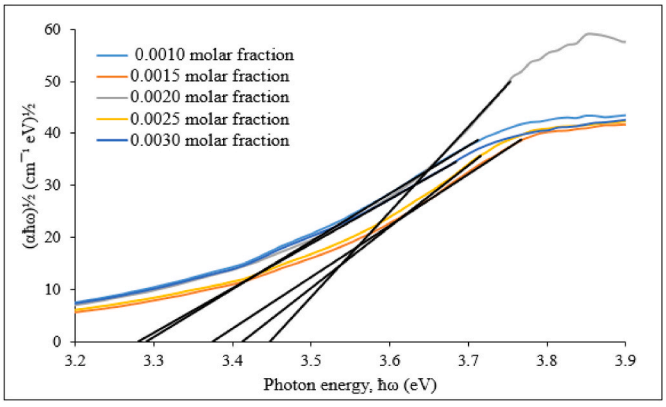

Fig. 7. Plot of $(\alpha\hbar\omega)^{1/2}$ against photon energy, ħω for $[\{[(TeO_2)_{0.7}\ (B_2O_3)_{0.3}]_{0.7}\ (ZnO)_{0.3}\}_{0.96}\ (La\ NPs)_{0.04}]_{1\text{-}y}\ (Au_2O_3)_y$ glasses.

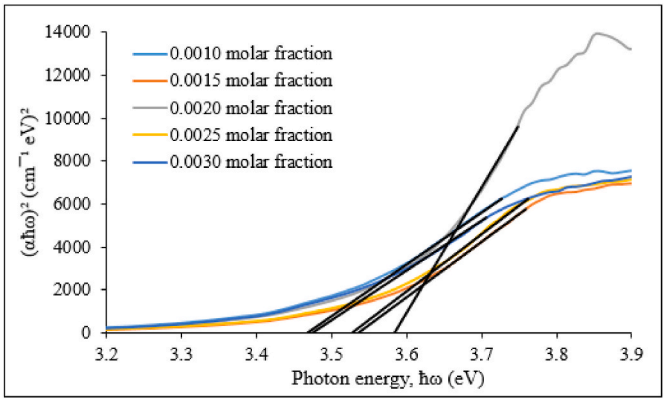

Fig. 8. Plot of $(\alpha\hbar\omega)^2$ against photon energy, ħω for $[\{[(TeO_2)_{0.7}\ (B_2O_3)_{0.3}]_{0.7}\ (ZnO)_{0.3}\}_{0.96}\ (La\ NPs)_{0.04}]_{1\text{-}y}\ (Au_2O_3)_y$ glasses.

Fig. 9 depicts the Urbach energy of zinc borotellurite glass doped with varying concentrations of gold oxide, while the corresponding values are presented in Table 3.

A decreasing trend in Urbach energy values is observed from 0.0010 to 0.0020 M fraction, signifying a negligible defect concentration inside the glass system [46]. The addition of gold oxide to the glass matrix, above a molar proportion of 0.0020, leads to increased Urbach energy values. The augmentation of ΔE value is associated with the escalating quantity of defects in the glass system [47]. A substantial defect in the

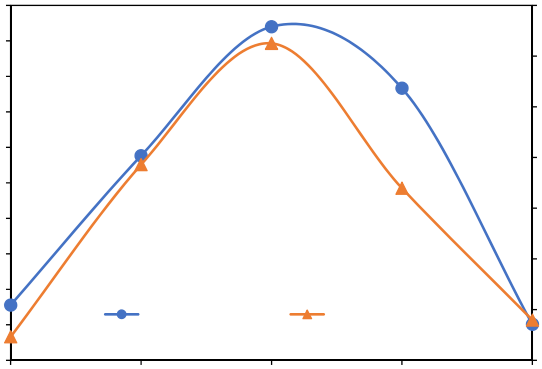

Fig. 9. Plot of indirect and direct transition of optical band gap for $[\{[(TeO_2)_{0.7}\ (B_2O_3)_{0.3}]_{0.7}\ (ZnO)_{0.3}\}_{0.96}\ (La\ NPs)_{0.04}]_{1\text{-}y}\ (Au_2O_3)_y$ glasses.

glass matrix may be linked to the increasing concentration of non-bridging oxygen resulting from bond cleavage inside the glass structure.

The increase in Urbach energy (ΔE) indicates greater structural disorder in the glass network, mainly due to defect formation. As the gold oxide content exceeds 0.0020 M fraction, more **non-bridging oxygens (NBOs)** are created due to bond cleavage in the tellurite and borate network, reducing connectivity and introducing localized energy states in the band gap. These defects facilitate low-energy electronic transitions, broadening the Urbach tail and increasing optical absorption. Gold oxide also acts as a **network modifier**, weakening structural integrity by increasing the ratio of NBOs to bridging oxygens, leading to more optical trap states that cause light scattering and absorption. Thermal fluctuations and compositional inhomogeneities further amplify these effects, affecting optical transparency. Therefore, optimizing gold oxide concentration is essential to enhance optical performance while minimizing defect-induced optical losses in photonic applications.

4.5. Refractive index

The refractive index is a critical metric examined to assess the suitability of glass materials for the optical systems. Numerous scholars have undertaken investigations to elucidate the relationship between the refractive index and the composition of glass [48]. The refractive index is determined using the subsequent equation:

$$\frac{n^2-1}{n^2+2}=1-\sqrt{\frac{Eopt}{20}} \tag{3.10}$$

where n is the refractive index and Eopt is the value for indirect band gap.

Fig. 10 depicts the refractive index of the analysed glasses. Table 4 shows the refractive indices for various concentrations of lanthanum oxide nanoparticles and gold oxide. The refractive index recorded varies from 2.28 to 2.33. The fluctuation in refractive index can be attributed to the disorder effect inside the glass system. Initially, the introduction of gold oxide at molar fractions ranging from 0.001 to 0.002 results in a reduction of the refractive index. The reduction of this phenomena can be attributed to the formation of TeO_{3+1} polyhedra from TeO_3 trigonal bipyramids within the glass network. The further incorporation of gold oxide up to a 0.003 M percentage suggests that the refractive index aligns with the emergence of non-bridging oxygen (NBO). This phenomenon is ascribed to the modification of the structural network resulting from the transformation of TeO_4 tbp to TeO_{3+1} tp, as evidenced by the findings related to the optical energy band gap. The structural alterations resulting from the disorderly arrangement caused by the

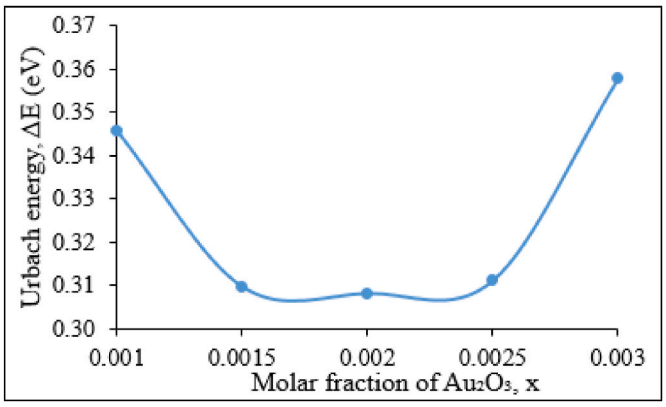

Fig. 10. Urbach energy for $[\{[(TeO_2)_{0.7}\ (B_2O_3)_{0.3}]_{0.7}\ (ZnO)_{0.3}\}_{0.96}$ (La NPs$)_{0.04}]_{1\text{-}y}$ $(Au_2O_3)_y$ glasses with different concentration of gold oxide. (For interpretation of the references to colour in this figure legend, the reader is referred to the Web version of this article.)

Table 4
The values of refractive index for $[\{[(TeO_2)_{0.7}\ (B_2O_3)_{0.3}]_{0.7}\ (ZnO)_{0.3}\}_{0.96}$ (La NPs$)_{0.04}]_{1\text{-}y}$ $(Au_2O_3)_y$ glasses.

Molar fraction, y	Refractive index, n
0.0010	2.3228
0.0015	2.3027
0.0020	2.2859
0.0025	2.2939
0.0030	2.3254

substitution of gold atoms. Gold atoms predominantly occupy interstitial positions, where there is compression towards the Te-O bond framework. As a result, gold atoms alter the initial Te-O bond length to a relative length, leading to an increase in lattice strain [42].

The relationship between the refractive index and the increase in gold oxide is due to the elevated density of gold oxide, as demonstrated in Fig. 4. The rise in the refractive index corresponds to the reduction of optical band gaps, as depicted in Fig. 8, which simultaneously leads to a greater number of non-bonding orbitals (NBO) with enhanced polarity relative to bonding orbitals (BO) [38,39].

4.6. Molar refraction (R_m), electronic polarizability (α_m), optical basicity (ˆ), and metallisation criterion (M)

Molar refraction (R_m) is a measure of the total polarizability of a mole for a substance. The values for molar refraction of glasses can be calculated using following relation [3.11]:

$$R_m = \left(\frac{n^2 - 1}{n^2 + 2}\right) V_m \tag{3.11}$$

where n is the refractive index and V_m is the molar volume of the glasses.

Meanwhile, the relation between electronic polarizability (α_m) and molar refraction (R_m) are expressed using formula [3.12]:

$$\alpha_m = \left(\frac{3}{4\pi N_A}\right) R_m \tag{3.12}$$

where N_A is the Avogadro's number (6.023×10^{23}).

Table 5 indicates that both molar refraction and electronic polarizability demonstrate a general decreasing tendency, with values ranging from 17.3597 to 16.7716 cm^3/mol and from 6.8888 to 6.6554 $\times 10^{(-24)}$ cm^3, respectively. The two patterns are associated with the diminishing quantity of non-bridging oxygens exhibiting high polarizability within the glass matrix as the concentration of Au_2O_3 rises.

Furthermore, the optical basicity is represented by the subsequent

Table 5
Molar refraction (R_m), electronic polarizability (α_m), optical basicity (ˆ), and metallisation criterion (M) for $[\{[(TeO_2)_{0.7}\ (B_2O_3)_{0.3}]_{0.7}\ (ZnO)_{0.3}\}_{0.96}$ (La NPs$)_{0.04}]_{1\text{-}y}$ $(Au_2O_3)_y$ glasses.

Molar fraction, y	R_m (cm^3/mol)	α_m (x 10^{-24} cm^3)	ˆ	M
0.0010	17.3597	6.8888	1.1231	0.4057
0.0015	17.0563	6.7684	1.1116	0.4108
0.0020	16.8371	6.6814	1.1028	0.4152
0.0025	16.7716	6.6554	1.0999	0.4131
0.0030	16.8537	6.6880	1.1028	0.4050

equation [3.13]:

$$= 1.67\left(1 - \frac{1}{\alpha o^{2-}}\right) \tag{3.13}$$

where αo^{2-} is the oxide ion polarizability of the glass samples.

The derived value for optical basicity is presented in Table 5. The optical basicity decreases from 1.1231 to 1.0999 with increasing Au_2O_3 content, indicating that the resulting glass samples possess acidic characteristics [49]. The declining trend may also be attributed to oxygen's diminishing capacity to transfer negative charge, leading to a reduction in oxygen polarizability.

The metallisation criteria (M) values assist in forecasting the metallic characteristics of a material, with R_m/V_m $>$ 1 indicating metallic materials and R_m/V_m $<$ 1 signifying non-metallic materials. The criterion for the metallisation of the glasses are established as follows [3.14]:

$$M = 1 - \frac{R_m}{V_m}, \tag{3.14}$$

The metallisation criterion values for lanthanum oxide nanoparticles doped zinc borotellurite glass system with the incorporation of gold oxide are documented in Table 5. The metallisation criterion for the prepared samples displays a consistent pattern with the optical band gap. The metallisation criteria rise from 0.4057 to 0.4152 as the concentration of Au_2O_3 escalates from 0.0010 to 0.0020 M fraction. As additional Au_2O_3 is incorporated, the M value diminishes until it attains a molar fraction of 0.0030. When the metallisation threshold is elevated, the valence and conduction bands are narrowed, resulting in greater optical band gap values and vice versa.

The discussion on practical applications of the synthesized glasses by including specific case studies where borotellurite-based and rare-earth-doped glasses have been successfully utilised in optoelectronic and photonic devices. For instance, **erbium-doped tellurite glasses** have been widely used in **erbium-doped fiber amplifiers (EDFAs)** for optical communication networks, where their high refractive index and broad transmission window improve signal amplification efficiency. Additionally, **lanthanum-doped glasses** have demonstrated suitability for **solid-state laser applications**, particularly in **Nd^{3+}** and **Yb^{3+} co-doped tellurite laser materials**, which are utilised in mid-infrared laser sources for medical diagnostics and remote sensing.

Furthermore, **gold-doped glasses** have been explored in **plasmonic photonic devices**, where their localized surface plasmon resonance (LSPR) effects enhance light-matter interactions, making them suitable for **nonlinear optical devices, optical waveguides, and all-optical switches** used in integrated photonic circuits. Research has also shown the potential of **gold oxide-doped borotellurite glasses** in **solar energy applications**, particularly in **photodetectors and solar concentrators**, where their tunable optical band gap improves light absorption and conversion efficiency. These case studies validate the relevance of the synthesized glass system and its potential for real-world applications in photonic and optoelectronic technologies.

4.7. Prediction using machine learning

In this section, machine learning was employed to predict the physical and optical properties of lanthanum and gold-doped zinc borotellurite glass, enabling a data-driven approach to material optimisation. The dataset utilised for machine learning training and evaluation was obtained from experimentally synthesized glass samples, as detailed in the previous section. The distinct glass compositions were used to train and evaluate the machine learning models, ensuring that all predictions were based on real experimental data and suit to apply in real scenarios. To ensure reliable model performance, an 80-20 train-test split was applied, where 80 % of the dataset was used for training, and 20 % was reserved for testing. Before training, data pre-processing was performed, including normalization of all input features to maintain consistency and prevent any single variable from dominating the learning process. Since all glass samples were experimentally measured, no missing values were present in the dataset.

The selection of input features was based on their physical significance and correlation with optical properties, ensuring that the models could accurately predict material behavior. The selected features included molar volume and density, which describe the atomic structure and packing efficiency of the glass matrix, and refractive index, direct band gap, indirect band gap, and Urbach energy, which define the optical properties of the material. These features were chosen because they directly influence the performance of glass in photonic and optoelectronic applications.

To further validate the importance of these features in model predictions, SHAP analysis was conducted. The results showed that molar volume and density had the strongest influence on refractive index and band gap variations, confirming their critical role in determining glass properties. By using experimentally derived data and selecting features based on both domain knowledge and statistical analysis, the machine learning models developed in this study provide a scientific and data approach to predicting and optimizing glass properties, where is one of the key novelties of this study for advancing glass technology in optoelectronics and photonics.

A simple hyperparameter tuning approach was applied to our models. For RF, the number of trees was varied between 100 and 500. GB and XGB were tuned with a learning rate between 0.01 and 0.1, and tree depth between 3 and 10 to optimize model generalization. ANN were configured with 3 hidden layers and 10 to 100 neurons per layer, using the ReLU activation function and Adam optimiser with basic learning rate adjustments. As this study serves as an initial exploration of ML for glass property prediction, default settings were used to achieve reliable results.

4.7.1. Prediction physical properties

Fig. 11 depicts the extensive results of forecasting the physical properties of materials, namely density and molar volume, employing several machine-learning models, including Random Forest (RF), Gradient Boosting (GB), XGBoost (XGB), and Artificial Neural Networks (ANN). Table 6provides a comparative comparison of R2 and RMSE for machine learning models in estimating material physical properties. The graphical and tabular metric comparison unequivocally reveals that RF has superior performance, achieving the highest R^2 score and the lowest RMSE value for forecasting density and molar volume. The RF model has a R^2 of 0.999997 and an RMSE of 0.000076 g/cm^3 for density, as well as impressive statistics for molar volume, with a R^2 of 0.999995 and an RMSE of 0.00058 cm^3/mol. These results highlight the model's ability to effectively detect intrinsic linear correlations, mostly due to advanced structuring techniques and adept handling of large data sets (see Table 7) (see Fig. 12).

The GB and XGB models exhibit strong predictive skills, with nearly identical R^2 values, indicating their effectiveness in generalising from training data. However, its slightly higher RMSE compared to RF suggests a modest reduction in accuracy, attributable to differences in data

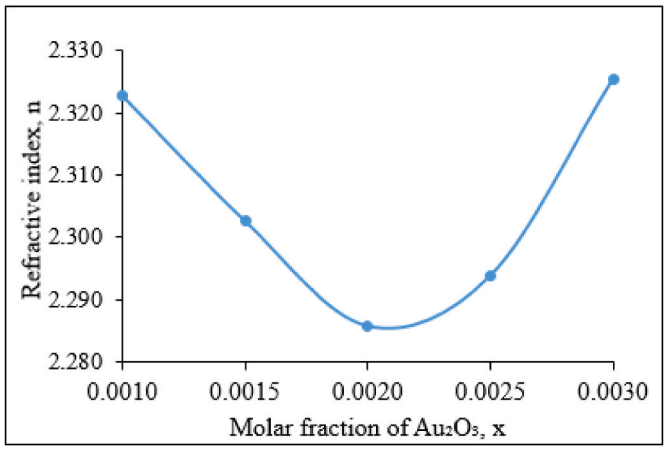

Fig. 11. Refractive index for $[\{[(TeO_2)_{0.7}\ (B_2O_3)_{0.3}]_{0.7}\ (ZnO)_{0.3}\}_{0.96}\ (La\ NPs)_{0.04}]_{1-y}\ (Au_2O_3)_y$ glasses with different concentration of gold oxide. (For interpretation of the references to colour in this figure legend, the reader is referred to the Web version of this article.)

simplicity management and model complexity. The ANN Model, albeit somewhat less effective than the ensemble method, exhibited robust prediction performance with an R2 of 0.998975 for density and 0.999923 for molar volume. The little decline in performance can be attributed to the inherent challenges of training neural networks, specifically the requirement for extensive datasets and thorough hyperparameter tuning.

4.7.2. Prediction optical properties

The results demonstrate the predictive accuracy of several machine learning models in forecasting intricate optical parameters, such as indirect and direct band gaps, Urbach energy, and refractive index. The data underscores the considerable effectiveness of ensemble methods, particularly Random Forest, in generating predictions with remarkable precision across diverse material characteristics. The RF model exhibits exceptional fidelity, with R2 scores consistently surpassing 0.99994 and remarkably low RMSE values (e.g., 0.000359 for the indirect band gap and 0.000085 for the refractive index), highlighting its effectiveness in accurately modelling the fundamental physical phenomena affecting these properties. This signifies a core advantage in employing advanced regularisation and loss approximation techniques inherent to RF, enhancing the accuracy and generalisability of forecasts in materials science applications. Moreover, while the ANN model exhibits competent performance, it slightly lags behind tree-based ensemble methods, especially in predicting band gaps, where its RMSE values, though modest, are much higher than those achieved by RF, GB, and XGBoost.

Fig. 13 illustrates the detailed results of predictions generated by various machine learning models, including Random Forest (RF), Gradient Boosting (GB), XGBoost (XGB), and Artificial Neural Networks (ANN), in assessing the physical properties of materials: Rm (cm3/mol), αm (x 10–24 cm^3), Lambda, and M. In this comparison, the ANN model demonstrates the least advantageous outcome, with only moderate efficacy for the other variables and insufficient forecasts for Lambda. This indicates that ANN may not be the most suitable choice for the current dataset. A negative R squared value for Lambda indicates that the model's predictions are less accurate than those derived from using the mean of the target values as the primary predictive variable. For instance, GB exhibits virtually impeccable predictions for variables like Lambda and M. The little variations in RMSE values suggest that it is slightly less accurate than RF, although remains very reliable. XG Boost, albeit a formidable model, demonstrates slightly diminished performance compared to RF and GB, particularly for the Lambda and M variables. Nevertheless, its R^2 values remain very close to 1, making it a reliable choice for most applications. The RF model demonstrates

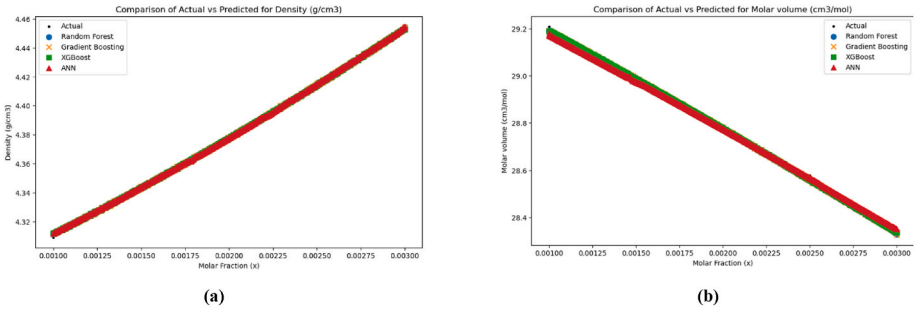

Fig. 12. Comparative Analysis of Machine Learning Models for Predicting Physical Properties of Materials (a) Density (g/cm^3) (b) Molar volume (cm^3/mol).

Table 6
Quantitative Performance Comparison of Machine Learning Models for Predicting (a) Density (g/cm^3) (b) Molar volume (cm^3/mol).

Model	Density (g/cm^3)		Molar volume (cm^3/mol)	
	R2	RMSE	R2	RMSE
RF	0.999997	0.000076	0.999995	0.00058
GB	0.999945	0.00307	0.999947	0.001816
XGB	0.999968	0.000234	0.999976	0.001216
ANN	0.998975	0.001319	0.999923	0.002184

exceptional performance across all variables, with virtually perfect R^2 values, signifying an ideal correlation between predicted and actual values. The exceptionally low RMSE values demonstrate that the model's predictions deviate insignificantly from actual values, confirming RF as the most reliable model in this analysis (see Fig. 14).

These results also emphasize RF's ability to effectively model nonlinear relationships and capture intricate dependencies between features, making it the most suitable choice for this dataset. The GB and XGB models also demonstrate strong predictive performance, with R^2 values close to 1. However, their slightly higher RMSE values indicate a minor decline in accuracy, likely due to their sensitivity and required extra hyperparameter tuning step and boosting mechanisms. These models sequentially adjust weights and iteratively refine predictions, making them more susceptible to overfitting when applied to complex materials datasets. Unlike RF, which aggregates independent decision trees in parallel, boosting models update trees iteratively, which can lead to greater instability if the training data is not sufficiently large or diverse. The ANN model, while capable of capturing nonlinear patterns, exhibited lower predictive accuracy compared to tree-based models. This discrepancy is attributed to ANN's reliance on larger datasets for generalization and its sensitivity to hyperparameter selection, which can lead to suboptimal weight updates when trained on relatively different datasets.

These findings correspond with the effectiveness of prior implementations utilising XGBoost and RF to improve accuracy in personality prediction derived from resumes [50]. The results in Ref. [50] demonstrate that the RF algorithm obtains an accuracy of 90 %, whereas XGBoost reaches an accuracy of 86 %, with a significance level of 0.846 ($p > 0.05$). This indicates that the hypothesis is statistically insignificant and was assessed using an independent samples T-test. Both the RF and XGBoost algorithms are highly efficient machine learning techniques for forecasting personality traits within the specified dataset.

The aforementioned results demonstrate the intrinsic benefits of employing a structured stacking technique and sophisticated loss estimates, which are crucial for RF, enhancing accuracy and prediction in materials science applications. Despite variations in performance related to the sensitivity of the neural network, comprehensive data training and hyperparameter optimisation can enhance the results of the ANN.

This illustrates the effectiveness of machine learning algorithms in understanding complex non-linear relationships within data sets, rendering them suitable for prediction and facilitating the discovery of whole new glass compositions. These findings are essential for the advancement of materials informatics, providing a range of reliable predictive tools that improve traditional experimental and theoretical methods. This expertise improves the understanding of material behaviour and accelerates the identification and application of novel materials with tailored characteristics. These results highlight the critical importance of selecting an appropriate machine learning model customised to the specific characteristics of the dataset and the expected physical properties. The RF model's outstanding performance in this study demonstrates its suitability for situations necessitating high

Table 7
Quantitative Performance Comparison of Machine Learning Models for Predicting (a) Density (g/cm^3) (b) Molar volume (cm^3/mol).

Model	Indirect band gap (eV)		Direct band gap (eV)		Urbach energy, ΔE (eV)		Refractive index, n	
	R2	RMSE	R2	RMSE	R2	RMSE	R2	RMSE
RF	0.99994	0.000359	0.999839	0.000373	0.999915	0.000136	0.99994	0.000085
GB	0.999774	0.000695	0.999666	0.000537	0.999761	0.000228	0.999778	0.000163
XGB	0.99985	0.000554	0.999733	0.00048	0.999784	0.000216	0.999806	0.000152
ANN	0.986775	0.005319	0.995576	0.001955	0.998873	0.000494	0.988556	0.001169

Table 8
Quantitative Performance Comparison of Machine Learning Models for Predicting Rm (cm^3/mol), αm (x 10-24 cm^3), Lambda and M.

Model	R_m (cm^3/mol)		α_m (x 10-24 cm^3)		Lambda		M	
	R2	RMSE	R2	RMSE	R2	RMSE	R2	RMSE
RF	1.0000	0.0003	1.0000	0.0001	1.0000	0.0000	0.9999	0.0000
GB	1.0000	0.0011	1.0000	0.0004	1.0000	0.0000	0.9998	0.0000
XGB	1.0000	0.0010	1.0000	0.0004	0.9999	0.0001	0.9997	0.0001
ANN	0.9456	0.0400	0.9918	0.0062	−0.0966	0.0071	0.4818	0.0020

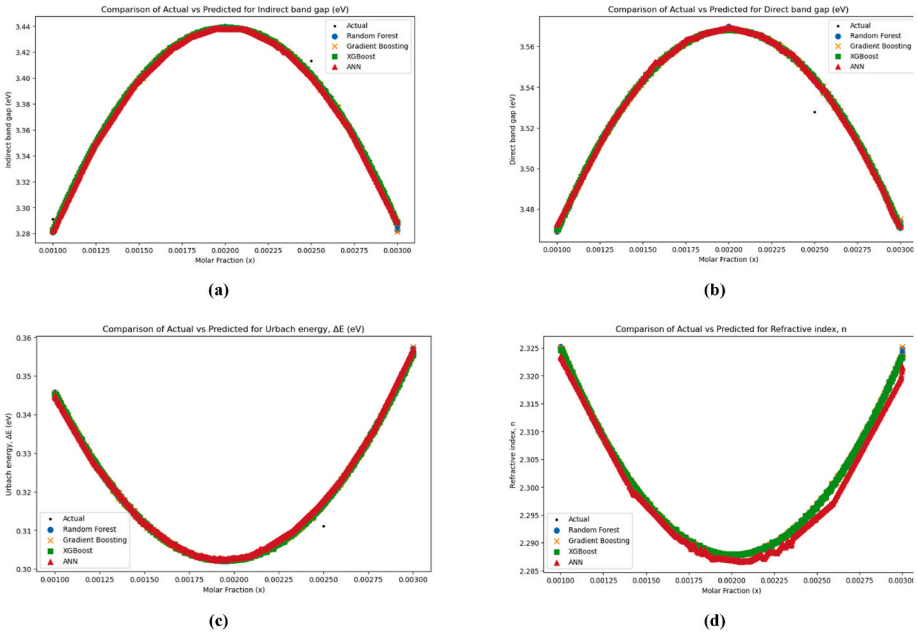

Fig. 13. Comparative Analysis of Machine Learning Models for Predicting Physical Properties of Materials (a) Density (g/cm^3) (b) Molar volume (cm^3/mol).

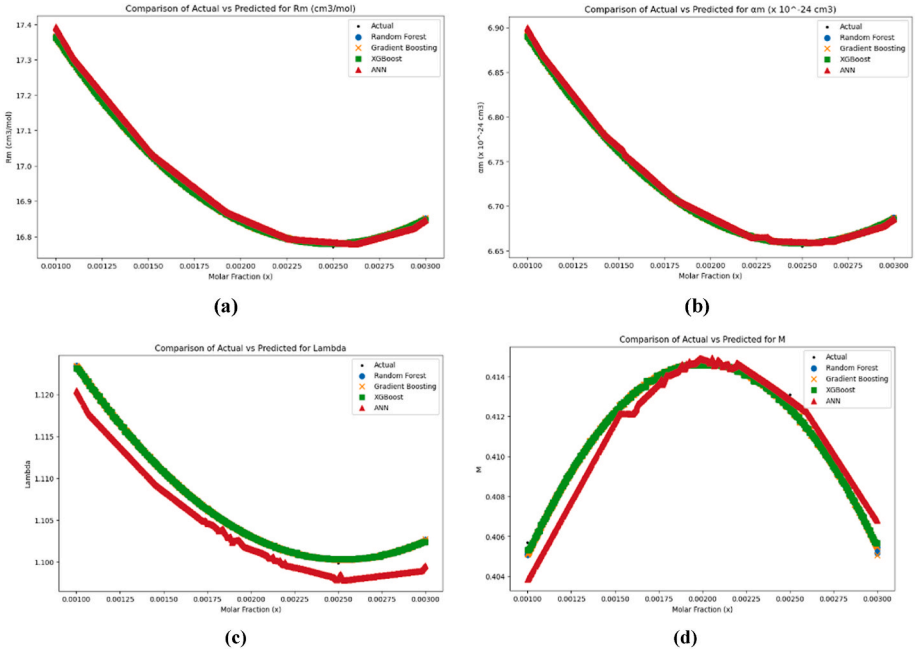

Fig. 14. Comparative Analysis of Machine Learning Models for Predicting Physical Properties of Materials (a) Density (g/cm3) (b) Molar volume (cm3/mol). Fig. 13. Comparative Analysis of Machine Learning Models for Predicting Physical Properties of Materials **(a)** Rm (cm^3/mol), **(b)** αm (x 10-24 cm^3), **(c)** Lambda, and **(d)** M.

precision and computational efficiency. This study serves as a benchmark for developing predictive models in materials science, demonstrating the potential of machine learning techniques to drive innovation in this field.

5. Conclusions

This study successfully synthesized gold oxide and lanthanum oxide nanoparticle-doped zinc borotellurite glasses with different amounts of gold oxide using the melt quenching technique. This study examines the effects of gold oxide on the structural, physical, and optical properties of the zinc borotellurite glass system. The XRD spectra of all the glasses had a pronounced hump at 20–30°, signifying that the glass samples have an amorphous structure. The absorption bands identified in the FTIR spectra at 663–669, 1056–1078, 1234–1244, and 1338-1352 cm^{-1} are associated with the vibrational modes of TeO_3, BO_4, and BO_3 units in the glass system. The density increases and molar volume decreases with the incorporation of additional gold oxide into the produced glass samples. The optical band gap exhibits two trends with rising concentrations of gold oxide. The optical band gap shows a growing trend from 0.0010 to 0.0020 M fraction, followed by a decrease with further additions of gold oxide up to 0.030 M fraction. The optical band gap values for indirect and direct transitions range from 3.2803 to 3.4480 eV and from 3.4693 to 3.5850 eV, respectively. The findings demonstrate that the Urbach

energy displays an inverse correlation with the optical band gap. The increase in the optical band gap and the decrease in Urbach energy values with higher gold oxide content can be ascribed to the formation of bridging oxygen and the improvement of the glass system's rigidity. The study established that the refractive index values of the glass ranged from 2.2859 to 2.3254. The decreasing molar refraction and electronic polarizability indicate that the glass samples demonstrate diminished polarisation as the concentration of bridging oxygen in the glass system rises. The optical basicity values reflect the acidic properties of the synthesized glasses. The metallisation criterion values range from 0.4050 to 0.4152, corresponding with the optical band gap pattern. The experimental findings were enhanced through four machine learning (ML) models: Random Forest (RF), Gradient Boosting (GB), XGBoost (XGB), and Artificial Neural Network (ANN), which accurately predicted density, molar volume, optical band gap, Urbach energy, and refractive index. Among these, RF outperformed other models due to its robust handling of nonlinear relationships and resistance to overfitting, while GB and XGB were more sensitive to hyperparameter tuning, and ANN underperformed due to data limitations and overfitting. The models effectively identified key properties trends, such as the increase in density and reduction in molar volume with rising gold oxide content and nonlinear fluctuations in optical band gap. These findings have significant implications for optoelectronic applications, accelerating the design of glass materials for optical fibers, solid-state lasers, and nonlinear photonic devices. The integration of the ML model not only validates the experimental results but also establishes a predictive framework for formulating new glass compositions with optimized optical characteristics for zinc borotellurite glasses co-doped with lanthanum oxide and gold oxide nanoparticles, which is crucial for future optical device applications. Future work should focus on advanced ML tuning techniques, exploring different dopants and glass systems, and integrating first-principles simulations (e.g., Density Functional Theory) with ML models to further refine property predictions.

CRediT authorship contribution statement

S.N. Nazrin: Writing – original draft, Methodology, Conceptualization, Formal analysis. **Camellia Doroody:** Conceptualization, Project administration, Writing – review & editing, Validation. **Liyana Adilla Burhanuddin:** Formal analysis, Writing – review & editing, Validation. **Neesha Jothi:** Conceptualization, Investigation, Validation. **N. Ibrahim:** Writing – review & editing, Validation. **Halimah Badioze Zaman:** Supervision, Validation. **M.H.M. Tahir:** Writing – review & editing, Validation. **Manzoore Elahi M. Soudagar:** Project administration, Writing – review & editing, Validation. **S. Ramesh:** Supervision. **Sagar Shelare:** Conceptualization. **Shubham Sharma:** Project administration, Funding acquisition, Validation.

Consent to participate

Not applicable.

Consent to publish

All authors have read and approved this manuscript.

Ethical approval

Not applicable.

Data availability statement

The data that support the findings of this study are available within the manuscript or from the main corresponding authors (SN Nazrin, and Camellia Doroody) who are primarily responsible for the thorough analysis, characterization testing, and experimentations. As all the characterizations, analysis, testing's related work and testing's have solely been responsible by SN Nazrin, and Camellia Doroody. Additionally, the raw data can be obtained on request from the corresponding authors, SN Nazrin, and Camellia Doroody.

Declaration of competing interest

The authors declare that they have no known competing financial interests or personal relationships that could have appeared to influence the work reported in this paper.

Acknowledgments

This work was supported by Tenaga Nasional Berhad (TNB) and UNITEN through Tan Sri Leo Moggie Chair of The Institute of Informatics and Computing in Energy, IICE under the code 2021EIChair.

References

[1] R.H. Doremus, Glass Science, 1973.
[2] S.R. Elliott, F.E.G. Henn, Application of the Anderson-Stuart model to the AC conduction of ionically conducting materials, J. Non-Cryst. Solids 116 (2–3) (1990) 179–190.
[3] A. Feltz, Amorphous Inorganic Materials and Glasses, VCH, 1993.
[4] A.K. Varshneya, Fundamentals of Inorganic Glasses, Acad. Press, New York, 1994.
[5] J.E. Shelby, J.J. Noonan, Formation and properties of sodium scandium silicate glasses, Phys. Chem. Glasses 38 (5) (1997) 251–255.
[6] P.J. Bray, Structural models for borate glasses, J. Non-Cryst. Solids 75 (1–3) (1985) 29–36.
[7] N.I. Ahmad, T.S. Kiong, C. Doroody, K.S. Rahman, M.N. Norizan, M.F. Ahmad, N. Amin, Copper doping effect in the back surface field layer of CdTe thin film solar cells, Alex. Eng. J. 88 (2024) 155–163.
[8] C. Doroody, K.S. Rahman, H.N. Rosly, M.N. Harif, K. Sopian, S.F. Abdullah, N. Amin, A comprehensive comparative study of CdTe thin films grown on ultra-thin glass substrates by close-spaced sublimation and RF magnetron sputtering, Mater. Lett. 293 (2021) 129655.
[9] S.N. Nazrin, M.K. Halimah, F.D. Muhammad, Comparison study of optical properties on erbium-doped and silver-doped zinc tellurite glass system for non-linear application, J. Mater. Sci. Mater. Electron. 30 (7) (2019) 6378–6389.
[10] M.K. Halimah, S.N. Nazrin, F.D. Muhammad, Influence of silver oxide on structural, physical, elastic and optical properties of zinc tellurite glass system for optical application, Chalcogenide Lett. 16 (8) (2019).
[11] A. Neumann, D. Walter, The thermal transformation from lanthanum hydroxide to lanthanum hydroxide oxide, Thermochim. Acta 445 (2) (2006) 200–204.
[12] P. Nandi, A. Srinivasan, G. Jose, Structural dependent thermal and optical properties of rare earth doped glass with mixed glass formers, Opt. Mater. 31 (4) (2009) 653–659.
[13] L.P. Naranjo, C.B. De Araújo, O.L. Malta, P.A.S. Cruz, L.R. Kassab, Enhancement of Pr^{3+} luminescence in PbO–GeO_2 glasses containing silver nanoparticles, Appl. Phys. Lett. 87 (24) (2005) 241914.
[14] L.R.P. Kassab, R.A. Kobayashi, M.J.V. Bell, A.P. Carmo, T. Catunda, Thermo-optical parameters of tellurite glasses doped with Yb^{3+}, J. Phys. Appl. Phys. 40 (13) (2007) 4073.
[15] K.C. Silva, O.A. Sakai, A. Steimacher, F. Pedrochi, M.L. Baesso, A.C. Bento, A. N. Medina, S.M. Lima, R.C. Oliveira, J.C.S. Moraes, K. Yukimitu, E.B. Araújo, M. Petrovich, D.W. Hewak, Temperature and wavelength dependence of the thermo-optical properties of tellurite and chalcogenide glasses, J. Appl. Phys. 102 (7) (2007) 073507.
[16] L.R.P. Kassab, F.A. Bomfim, J.R. Martinelli, N.U. Wetter, J.J. Neto, C.B. de Araújo, Energy transfer and frequency upconversion in Yb^{3+}–Er^{3+}-doped PbO-GeO_2 glass containing silver nanoparticles, Appl. Phys. B 94 (2) (2009) 239–242.
[17] A.F.L. Almeida, R.R. Silva, H.H.B. Rocha, P.B.A. Fechine, F.S.A. Cavalcanti, M. A. Valente, F.N.A. Freire, R.S.T.M. Sohn, A.S.B. Sombra, Experimental and numerical investigation of a ceramic dielectric resonator (DRA): $CaCu_3Ti_4O_{12}$ (CCTO), Phys. B Condens. Matter 403 (4) (2008) 586–594.
[18] B.F. Lu, J.F. Li, L.T. Kong, Y.H. Zhou, Correlation between mechanical behavior and glass forming ability of Zr–Cu metallic glasses, Intermetallics 19 (7) (2011) 1032–1035.
[19] S. Qu, Y. Zhang, H. Li, J. Qiu, C. Zhu, Nanosecond nonlinear absorption in Au and Ag nanoparticles precipitated glasses induced by a femtosecond laser, Opt. Mater. 28 (3) (2006) 259–265.
[20] T. Tokizaki, A. Nakamura, S. Kaneko, K. Uchida, S. Omi, H. Tanji, Y. Asahara, Subpicosecond time response of third-order optical nonlinearity of small copper particles in glass, Appl. Phys. Lett. 65 (8) (1994) 941–943.
[21] M.F. Faznny, M.K. Halimah, A.A. Latif, I.S. Mustafa, Synthesis and optical characterization of zinc borotellurite glass doped with lanthanum nanoparticles, Solid State Phenom. 268 (2017) 23–27. Trans Tech Publications Ltd.

[22] D. Schletz, M. Breidung, A. Fery, Validating and utilizing machine learning methods to investigate the impacts of synthesis parameters in gold nanoparticle synthesis, J. Phys. Chem. C (2023).
[23] M. Fronzi, R.D. Amos, R. Kobayashi, N. Matsumura, K. Watanabe, R.K. Morizawa, Evaluation of machine learning interatomic potentials for the properties of gold nanoparticles, Nanomaterials 12 (2022).
[24] S.A. Ahmad, H.U. Ahmed, D.A. Ahmed, B.H.S. Hamah-ali, R.H. Faraj, S.K. Rafiq, Predicting concrete strength with waste glass using statistical evaluations, neural networks, and linear/nonlinear models, Asian J. Civil Eng. 24 (8) (2023) 3023–3035.
[25] O. M'hamdi, S. Takács, G. Palotás, R. Ilahy, L. Helyes, Z. Pék, A comparative analysis of XGBoost and neural network models for predicting some tomato fruit quality traits from environmental and meteorological data, Plants 13 (5) (2024) 746.
[26] V. Paranthaman, K.S. Devi, K.B. Bhojanaa, V. Aravindan, G. Raman, R.S. Kumar, P. S. Krishnan, Experimental and theoretical insights into enhanced light harvesting in dye-sensitized solar cells via Au@ TiO2 core-shell and BaTiO3 nanoparticles, J. Taiwan Inst. Chem. Eng. 165 (2024) 105778.
[27] C. Doroody, T.S. Kiong, S. Darzi, Sinr improvement using firefly algorithm (fa) for linear constrained minimum variance (lcmv) beamforming technique, in: 2015 International Conference on Computer, Communications, and Control Technology (I4CT), IEEE, 2015, April, pp. 441–445.
[28] F. Mohd Fudzi, H. Mohamed Kamari, A. Abd Latif, A. Muhammad Noorazlan, Linear optical properties of zinc borotellurite glass doped with lanthanum oxide nanoparticles for optoelectronic and photonic application, J. Nanomater. 2017 (2017).
[29] G. Lusvardi, G. Malavasi, V. Aina, L. Bertinetti, G. Cerrato, G. Magnacca, C. Morterra, L. Menabue, Bioactive glasses containing Au nanoparticles. Effect of calcination temperature on structure, morphology, and surface properties, Langmuir 26 (12) (2010) 10303–10314.
[30] M.F. Faznny, M.K. Halimah, M.N. Azlan, Effect of lanthanum oxide on optical properties of zinc borotellurite glass system, J. Optoelectr. Biomed. Mater. 8 (2) (2016) 49–59.
[31] A. Amat, H. Mohamed Kamari, C. Abdullah, C. Azurahanim, M. Ishak, I.S. Mustafa, S. Abdul Aziz, Optical properties changes of ternary glasses: gamma irradiation effect, Mater. Sci. Forum 840 (2016) 118–123. Trans Tech Publications Ltd.
[32] B. Karthikeyan, C.S. Suchand Sandeep, J. Cha, H. Takebe, R. Philip, S. Mohan, Optical properties and ultrafast optical nonlinearity of Yb^{3+} doped sodium borate and bismuthate glasses, J. Appl. Phys. 103 (10) (2008) 103509.
[33] O. Ravi, C.M. Reddy, L. Manoj, B.D.P. Raju, Structural and optical studies of Sm^{3+} ions doped niobium borotellurite glasses, J. Mol. Struct. 1029 (2012) 53–59.
[34] K. Nanda, R.S. Kundu, S. Sharma, D. Mohan, R. Punia, N. Kishore, Study of vibrational spectroscopy, linear and non-linear optical properties of Sm^{3+} ions doped $BaO–ZnO–B_2O_3$ glasses, Solid State Sci. 45 (2015) 15–22.
[35] G. Lakshminarayana, K.M. Kaky, S.O. Baki, A. Lira, P. Nayar, I.V. Kityk, M. A. Mahdi, Physical, structural, thermal, and optical spectroscopy studies of $TeO_2–B_2O_3–MoO_3–ZnO–R_2O$ (R= Li, Na, and K)/MO (M= Mg, Ca, and Pb) glasses, J. Alloys Compd. 690 (2017) 799–816.
[36] I. Kashif, A.A. El-Maboud, A. Ratep, Effect of Nd_2O_3 addition on structure and characterization of lead bismuth borate glass, Results Phys. 4 (2014) 1–5.
[37] M.K. Halimah, M.F. Faznny, M.N. Azlan, H.A.A. Sidek, Optical basicity and electronic polarizability of zinc borotellurite glass doped La^{3+} ions, Results Phys. 7 (2017) 581–589.
[38] A. Awang, S.K. Ghoshal, M.R. Sahar, M.R. Dousti, R.J. Amjad, F. Nawaz, Enhanced spectroscopic properties and Judd–Ofelt parameters of Er-doped tellurite glass: effect of gold nanoparticles, Curr. Appl. Phys. 13 (8) (2013) 1813–1818.
[39] G. Jagannath, B. Eraiah, K. NagaKrishnakanth, S.V. Rao, Linear and nonlinear optical properties of gold nanoparticles doped borate glasses, J. Non-Cryst. Solids 482 (2018) 160–169.
[40] P.G. Pavani, K. Sadhana, V.C. Mouli, Optical, physical and structural studies of boro-zinc tellurite glasses, Phys. B Condens. Matter 406 (6) (2011) 1242–1247.
[41] S.S. Hajer, M.K. Halimah, Z. Azmi, M.N. Azlan, Optical properties of zinc borotelluite doped samarium, Chalcogenide Lett. 11 (11) (2014).
[42] S.Q. Mawlud, Optical properties of tellurite glasses embedded with gold nanoparticles, in: Tellurite Glass Smart Materials, Springer, Cham, 2018, pp. 105–142.
[43] A. Rajabi, Y. Boon Kar, C. Doroody, T. Sieh Kiong, N.A. Arzaee, M.F. Mohamad Noh, M.J. Ghazali, Physiochemical and electrical activities of nano copper oxides synthesised via hydrothermal method utilising natural reduction agents for solar cell application, Nanotechnol. Rev. 13 (1) (2024) 20240008.
[44] R.H.C. Wui, A. Awang, A.L.S. Voi, C.F. Pien, N. Abdullah, J. Dayou, Tuning optical properties of erbium-doped zinc-sodium tellurite glass via incorporation of gold nanoparticles, Trans. Sci. Technol 4 (3) (2017) 209–217.
[45] S.B. Kolavekar, N.H. Ayachit, G. Jagannath, K. NagaKrishnakanth, S.V. Rao, Optical, structural and Near-IR NLO properties of gold nanoparticles doped sodium zinc borate glasses, Opt. Mater. 83 (2018) 34–42.
[46] S. Rani, S. Sanghi, A. Agarwal, V.P. Seth, Study of optical band gap and FTIR spectroscopy of Li_2O-Bi_2O_3-P_2O_5 glasses, Spectrochim. Acta Mol. Biomol. Spectrosc. 74 (3) (2009) 673–677.
[47] A.S. Asyikin, M.K. Halimah, A.A. Latif, M.F. Faznny, S.N. Nazrin, Physical, structural and optical properties of bio-silica borotellurite glass system doped with samarium oxide nanoparticles, J. Non-Cryst. Solids 529 (2020) 119777.
[48] R. El-Mallawany, The optical properties of tellurite glasses, J. Appl. Phys. 72 (5) (1992) 1774–1777.
[49] R. Bobbili, Interpretable glass forming ability prediction of amorphous alloys through tree based algorithms, Mater. Lett. 349 (2023) 134774.
[50] K.M. Reddy, R.T. Prabu, Machine learning approach for personality prediction from resume using XGBoost classifier and comparing with novel random Forest Algorithm to improve accuracy. 2023 Eighth International Conference on Science Technology Engineering and Mathematics (ICONSTEM), 2023, pp. 1–7.